PHYSICS OF FLUIDS **26**, 053304 (2014)

Positron emission tracking of individual particles in particle-laden rimming flow

P. Denissenko,[1,a)] E. Guyez,[2,b)] P. J. Thomas,[1,c)] D. J. Parker,[3,d)] and J. P. K. Seville[4,e)]

[1]*Fluid Dynamics Research Centre, School of Engineering, University of Warwick, Coventry CV4 7AL, United Kingdom*
[2]*CEA DEN, 17 rue des Martyrs, 380 Grenoble, France*
[3]*School of Physics and Astronomy, University of Birmingham, Birmingham B15 2TT, United Kingdom*
[4]*Department of Chemical and Process Engineering, University of Surrey, Guildford GU2 7XH, United Kingdom*

(Received 3 July 2013; accepted 1 May 2014; published online 27 May 2014)

The motion of a single tracer particle in particle-laden rimming flows is investigated experimentally by means of Positron Emission Particle Tracking (*PEPT*). Semi-dilute suspensions, with a volume fraction of 8% of heavy particles are considered. The trajectory of the tracer particle is monitored for several thousand cylinder revolutions and related to the optically recorded drift of the large-scale granular segregation bands developing in the cylinder. Results of the data analysis provide first insights into the relation between behaviour of individual particles and the spatiotemporal dynamics displayed by the macroscopic particle-segregation patterns. © *2014 AIP Publishing LLC*. [http://dx.doi.org/10.1063/1.4876383]

I. INTRODUCTION

Flows of fluids, granules, or particle-liquid mixtures contained inside horizontal rotating cylinders can display a wide variety of dynamic scenarios. Experimental results obtained with the conceptually simple rotating drum arrangement have made major contributions to the understanding of the fundamental physics governing many complex systems (Seiden and Thomas[1]).

Here we report new experimental results for the flow dynamics inside a horizontally rotating cylinder partially filled with a particle-laden liquid. The rotating-cylinder flow geometry illustrated in Fig. 1 is commonly referred to as rimming flow. When the cylinder rotates with low angular velocity, ω, its rising side pulls a thin liquid film out of the recirculating pool and this film covers the inner cylinder surface as shown in the figure. At sufficiently high rotation rates all liquid from the pool gets redistributed into the film covering the inner cylinder surface and this flow state is known as the rimming state. Here we consider regimes where the pool at the bottom of the cylinder still exists. Suspensions containing particles with a density higher than that of the carrier liquid are used.

The first studies of rimming flow of a homogeneous, i.e., particle free, liquid were conducted by Malkin[2,3] in order to model the flow of condensate in paper machine dryers under operating conditions. However, in the early 1990s rimming flow began to attract the attention of scientists interested in issues related to the fundamental physics underlying pattern formation phenomena.[1] Results of Melo[4] on flow patterns displayed by rimming flows of homogeneous liquids motivated Boote and Thomas[5] to investigate how granular additives affect the transition boundaries between the different flow patterns in phase space. One surprising result of their study was the observation

a)P.Denissenko@gmail.com. URL: http://www.warwick.ac.uk/pdenissenko
b)Estelle.Guyez@cea.fr
c)PJT1@eng.warwick.ac.uk
d)D.J.Parker@bham.ac.uk
e)J.P.K.Seville@surrey.ac.uk

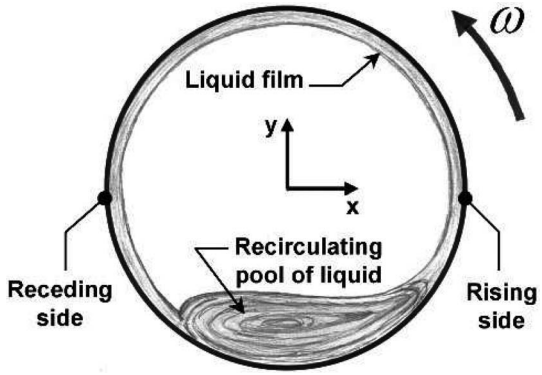

FIG. 1. Cross section of horizontal rotating cylinder illustrating rimming flow.

that granules, which are initially uniformly distributed throughout the liquid, segregate to form a set of regularly spaced particle-rich annular bands separated by regions of liquid almost entirely free of the granules. An example of this banding pattern is shown in Fig. 2 where the rising side (cf. Fig. 1) of the horizontal cylinder is shown. While the particular photo of segregation bands shown in Fig. 2 was obtained with particles denser than the carrier liquid, similar banding patterns also form with neutrally buoyant particles (see, e.g., Jin and Acrivos[13,14] and Tirumkudulu[16]) and with particles which are lighter than the carrier liquid (see, e.g., Thomas *et al.*[8]).

The long term observations of Guyez and Thomas[6,7] revealed that the segregation bands can drift along the axis of rotation displaying a spatiotemporal behaviour with different, sometimes very complex but highly symmetric, drift modes. An example of this spatiotemporal behaviour is illustrated in Fig. 3 which displays data for an experiment running over 1.5 days. The abscissa of Fig. 3 represents the position along the cylinder. The location of the left end wall of the cylinder corresponds to $L = 0$ cm and the right end wall is at $L = 27$ cm. The ordinates of the figure display time in terms of cylinder revolutions t/T (t is time; T is the cylinder rotation period) on the left and in days on the right. The positions of bands of particles are identified by the black regions. The figure reveals that the segregation bands from the left half of the cylinder drift towards the left end wall while the bands in the right half drift towards the right end wall. The origins of black lines—in Fig. 3 best resolved near the central region of the cylinder—identify locations where new bands form, replacing those vanishing at the end walls. Other space-time diagrams in Refs. 6 and 7 illustrate that band pattern can adopt many fundamentally different modes of evolution. Depending on the

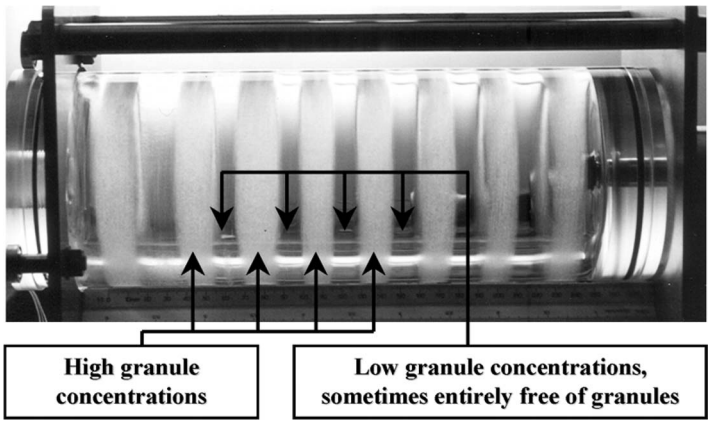

FIG. 2. Segregation-band pattern. Reprinted with permission from Guyez and Thomas, Phys. Fluids **21**, 033301 (2009). Copyright 2009 American Institute of Physics.[7]

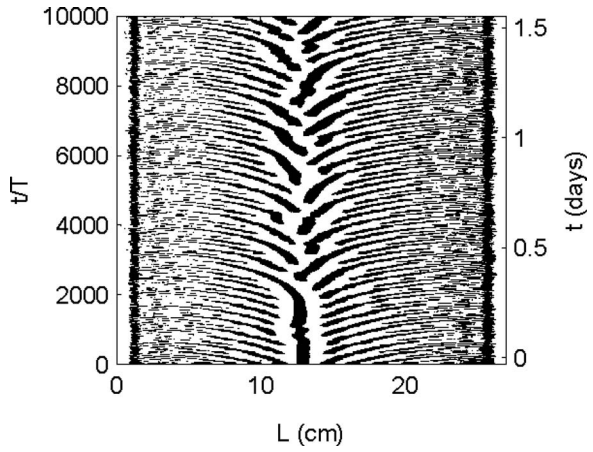

FIG. 3. Spatiotemporal diagram illustrating one characteristic band-drift mode. Black areas correspond to bands drifting towards cylinder end walls. Reprinted from Guyez and Thomas, Phys. Rev. Lett. **100**, 074501 (2008). Copyright 2008 American Physics Society.[6]

experimental conditions, bands can drift inwards or outwards, they can display zigzag motion, bands can split or merge, undergo irregular oscillations, or remain stationary.

The studies of Guyez and Thomas[6,7] have already identified regions of the parameter space where some of the drift modes are encountered. However, their studies could not establish the origin of the band drift and neither does there exist any information on how the phase-space dynamics of individual particles relate to the global band-drift mode adopted by the system. In order to begin answering these questions we have performed a series of experiments using the *Positron Emission Particle Tracking* (*PEPT*) facility at the University of Birmingham. The *PEPT* technique was invented at Birmingham and it enables the tracking of a single radioactively tagged tracer particle, among thousands of other similar particles, in the liquid inside the rotating cylinder. Since the mechanical properties of the tracer particle remain unaffected by tagging, monitoring a sufficiently long interval of its trajectory enables conclusions to be drawn regarding the behaviour of the entire particle population within the cylinder. Here we report first results obtained from the analysis of our *PEPT* data.

II. EXPERIMENTAL SET UP AND TECHNIQUES

The rotating drum facility used in the present study is the same as that used in our previous studies and it is described in detail in Refs. 5–8. Briefly, the facility consists of a transparent cylinder with radius $R = 50$ mm and length $L = 270$ mm that can be rotated with prescribed angular velocity ω around a horizontal axis (cf. Figs. 1 and 2). The cylinder aspect ratio is thus $L/R = 5.4$. The directions horizontally and vertically across the cylinder's cross-section are referred to by x and y as illustrated in Fig. 1 and the z-coordinate direction points along the axis of rotation with the end walls of the cylinder at $z = 0$ and $z = 270$ mm. The cylinder is filled with a particle-laden liquid to 14% of its volume and the particles constitute 8% of the volume of the suspension in all the experiments.

The experimental parameters are summarised in Table I. The fluid used was silicone oil (Ambersil, F111) with the density of $\rho_f \approx 0.97$ g cm^{-3} and surface tension $\sigma = 0.021$ N m^{-1} at room temperature. The kinematic viscosity of the oil varied from $\nu = 55$ cSt to $\nu = 1000$ cSt. The particles used were spherical glass beads of density $\rho_g = 2.5$ g cm^{-3}. Their mean radius was $r_p = 170$ μm for the *PEPT* experiments described in Sec. III. For these experiments, the cylinder rotation rate was chosen to keep the ratio of the particle sink rate to the cylinder surface velocity constant at a value characterized by the Stokes number of $St = V_s/\omega R = \frac{2}{9} g(\rho_p - \rho_f) r_p^2/\mu\omega R \cong 0.008$. For the experiments on the band growth rate, described in Sec. V, we have also used particles with the mean radius $r_p = 80\,\mu$m.

TABLE I. The experimental parameters. The runs identified by the prefix PT represent *PEPT* experiments. The runs with prefix BG were recorded on video only and analysed to evaluate the band growth rate. The rotation rate f of the cylinder is given in revolutions per minute. Constant during all experiments are: cylinder aspect ratio, $L/R = 5.4$; filling fraction, 14%; particle volume fraction, 8%; the capillary number, $\sigma/\rho g R^2 = 0.00088$.

Run	f, rpm	ν, cSt	r_p, μm	$\mathrm{Re}_h = \omega h_m^2/\nu$	$\alpha = \sqrt{\omega\nu/gR}$	$h_{min}/2r_p$	St
PT#1, 2	2.5	1000	170	0.0032	0.0231	2.03	0.00758
PT#3	8.2	295	170	0.036	0.0227	1.99	0.00784
PT#4	11.4	210	170	0.070	0.0226	1.98	0.00792
PT#5	24	100	170	0.31	0.0226	1.98	0.00790
PT#6	44	55	170	1.0	0.0227	1.99	0.00783
BG#38 . . . 45	3.2 . . . 34	500	170	0.0082 . . . 0.087	0.018 . . . 0.06	1.6 . . . 5.3	0.012 . . . 0.0011
BG#47 . . . 54	2.2 . . . 34	500	80	0.0056 . . . 0.087	0.015 . . . 0.06	2.9 . . . 11	0.0038 . . . 0.00025

The governing dimensional and nondimensional parameters of the system are discussed in detail in Ref. 7. Generally there are eight relevant nondimensional parameters. Seven of these were originally identified in Refs. 13 and 14 who dealt with rimming flows of neutrally buoyant particles and Guyez and Thomas[7] added an eighth parameter to account for the effects introduced by the different density of the particles and the liquid.

As discussed in Ref. 7 several of the dimensional parameters appear in a number of different nondimensional groups simultaneously. This renders it difficult to perform a complete systematic exploration of the phase-space dynamics subject to the variation of each of the nondimensional groups individually. For the *PEPT* results described here in Sec. III only the Reynolds number Re_h, based on the mean thickness of the liquid film on the inner cylinder wall, changes among the nondimensional parameters listed in Table I. For the experiments on band formation, discussed in Sec. V, particles with different mean radii ($r_p = 80\,\mu$m and $r_p = 170\,\mu$m) were used, the fluid viscosity was kept constant, and the rotational velocity was 2.4 rad s$^{-1} \le \omega \le$ 27.3 rad s^{-1}. These variations effect four of the eight nondimensional groups simultaneously. The groups affected are (i) the Reynolds number, (ii) the ratio of viscous and gravitational forces, (iii) the ratio between the minimum liquid-film thickness covering the inner cylinder wall and the particle diameter, and (iv) the Stokes number indicating the ratio of the particle sink rate to the cylinder rotation speed. For further details of the system behaviour in different regions of the nondimensional parameter space refer to Ref. 7.

Parameters of the system used for the *PEPT* study were chosen based on the experience gained from our previous experiments[5–8] to ensure, *a priori*, that the runs would result in sufficiently complex band dynamics making the study worthwhile. As *PEPT* experiments are expensive to run, and the rimming-flow experiments take a day for each set of parameters, it was decided to vary only the cylinder rotation speed and adjust the liquid viscosity keeping the ratio of the particle sink rate and the speed of the cylinder surface constant (i.e., $St = const$).

The *PEPT* technique relies on tagging one of the glass particles with a radioactive isotope before introducing it into the cylinder that contains silicone oil with the remaining particles. Details regarding the *PEPT* technique are summarized in Refs. 9–11. Briefly, the *PEPT* method is based on the detection of photons emitted when a positron, produced by the beta decay of an unstable nucleus, annihilates with an electron. Our rimming-flow apparatus is shown between the two *PEPT* detectors in Fig. 4. During the annihilation process following the beta decay, a pair of photons is emitted in opposite directions (180° apart). The photons are then detected simultaneously by the two detectors in Fig. 4 positioned opposite each other. Upon their detection it is known that the positron-electron annihilation occurred somewhere along the straight path line of the photons connecting their known impact locations on the two detectors. A number of such detection events occurring in sufficiently quick succession, such that the particle position has not changed appreciably, define a set of lines intersecting at the location of the beta decays, which is the location of the tagged glass bead. The data rate allows location of the particle with a precision better than 1 mm at the speed of 10 m s^{-1} and an increased precision of better than the particle size at the low velocities associated with the cylinder rotation in our *PEPT* experiments.

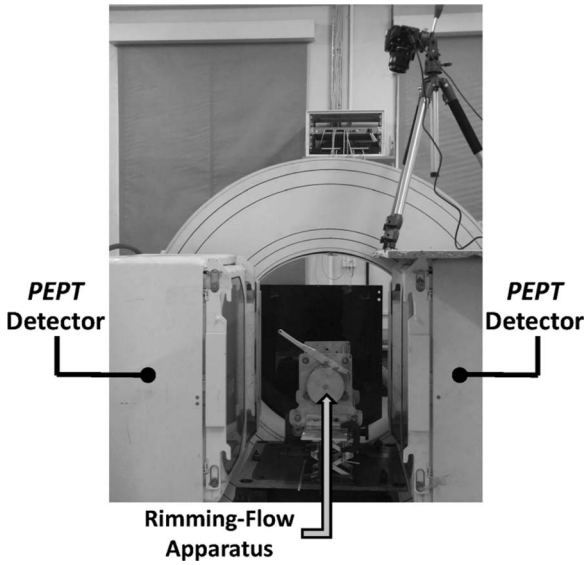

FIG. 4. The rimming-flow apparatus (cylinder extending into plane of photo) positioned between the two detectors of the *PEPT* facility at Birmingham.

The recorded *PEPT* particle trajectories were down sampled to track the particle position with a resolution of 50 sampling points per cylinder revolution. This procedure was performed to reduce the size of data sets so that they could be handled by MATLAB. A typical plot of a particle trajectory recorded for the time interval of approximately 4 h, is shown in Fig. 5. The grey (red online) segments of the trajectory represent the particle being entrapped within a granular band while the black (blue online) segments represent it while remaining within the pool. Note that the same colour coding will be employed throughout the manuscript.

Due to the density difference between the glass particles and the less dense silicon oil, the particles are subject to a gravity-driven Stokesian sedimentation. Using the classic formula (see, e.g., Batchelor,[12] p. 234) we determined sedimentation velocities in the range of $20\,\mu\mathrm{m s}^{-1} \leq V_s$

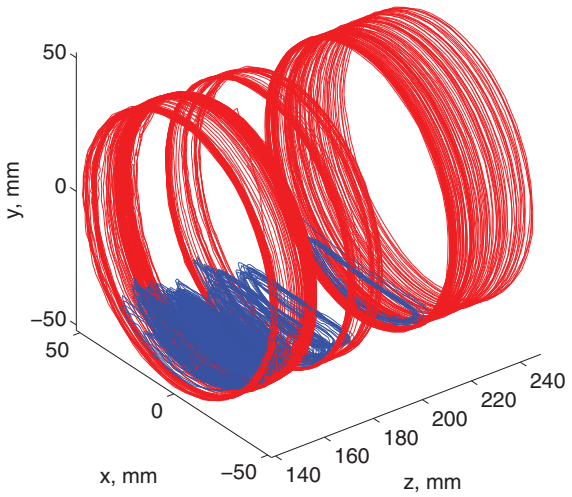

FIG. 5. A typical trajectory of the radioactively tagged particle for a time interval of approximately 4 h, or 2000 drum revolutions (run PT#3). Grey (red online) segments: particle entrapped within a granular band; black (blue online) segments particle within recirculating pool.

$\leq 400\,\mu\mathrm{ms}^{-1}$ for our experiments. The fluid viscosity is chosen in such a way that the ratio of sink rate to the speed of the cylinder surface, a characteristic velocity in the system, is constant at $V_{sink}/\omega R \approx 0.008$. As this ratio is small, it can be assumed that the velocity of the tagged particle represents the local fluid velocity.

III. RESULTS OF PEPT TRACKING

Figure 6 displays a typical set of graphs showing the x, y, and z coordinates of a radioactively tagged particle as a function of time t. Those parts of trajectories where x and y span the whole range from $-R$ to $+R$ identify intervals where the particle is trapped inside a granular band while those segments with reduced ranges of x and y correspond to intervals when the particle stays within the liquid pool.

The detailed analysis of the particle trajectory recorded by *PEPT* has revealed that in the vast majority of cases the particle escapes from granular bands inside a droplet that detaches from the liquid film near the top of the cylinder and falls down into the liquid pool. Such events can be identified in Fig. 6(b) as discontinuities on the time series of the y coordinate and are indicated by circular markers. The existence of this type of droplet was briefly referred to in Ref. 7 but not discussed any further.

Figure 7 shows the particle trajectory in the $x - y$ plane. The figure shows that, while travelling within a band, the particle passes underneath the pool. It enters the sub-pool region near the point $x \approx -35$ mm, $y \approx -35$ mm and re-emerges from it near $x \approx 38$ mm, $y \approx -30$ mm. The black (blue online) segment of the trajectory in Fig. 7 moreover reveals that the tagged particle did not enter the central core region of the recirculating pool located in the vicinity of -1 mm $< x <$ 10 mm and -45 mm $< y < -40$ mm. Finally, Fig. 7 does not display any evidence of events where the particle escaped from granular bands while passing the sub-pool region. This appears surprising since one might intuitively expect that the flow dynamics at the bottom of the cylinder is responsible for triggering and mediating the escape of particles from granular bands. The grey (red online) lines in Fig. 7 running slightly inclined from the top of the cylinder towards its lower half correspond to those parts of the trajectory when the particle was contained within a liquid drop falling from a granular band into the liquid pool, i.e., they represent events such as those highlighted by the circular markers on the time series of the y coordinate in Fig. 6(b). The small loops, such as that marked by the straight arrow on the rising side ($x > 0$) of the cylinder near its top, identify droplets that have nearly detached from the liquid film, slipped downwards at the film surface, and were then re-entrained by the band. Unlike the escape of a particle from a band—inside a falling droplet—the

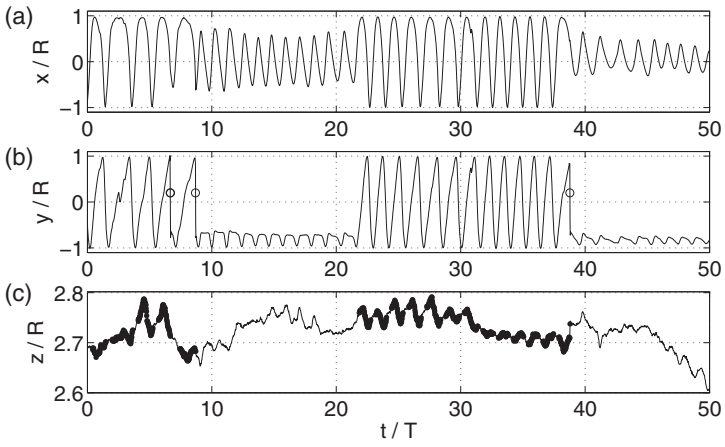

FIG. 6. Typical *PEPT* time series of the x, y, and z coordinates of the particle (run PT#1). Coordinates are normalised by the cylinder radius R while time is normalised by the cylinder revolution period T. Parts of the particle trajectory located above the pool surface are highlighted in plot (c) for the z component. Events when the particle leaves the band by falling into the pool, presumably within a droplet detaching from the cylinder wall, are marked by circles in (b) on the $y(t)$ graph.

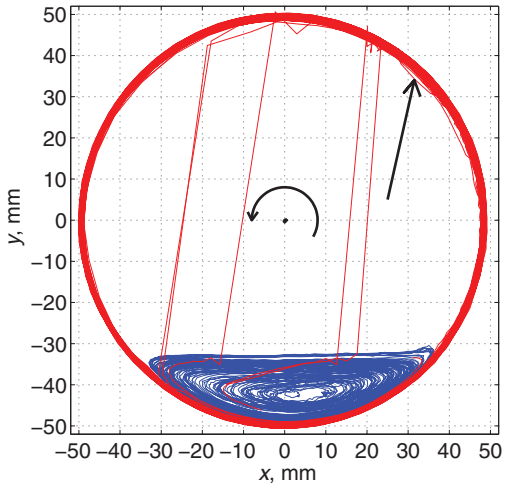

FIG. 7. A typical plot of the particle trajectory in the $x - y$ plane (cross-section). Note the parts of the trajectory corresponding to instances when the particle descends within an oil droplet from the region near the top of the cylinder down towards and into the pool. These events are also marked by circles in Fig. 6(b).

particle entrainment into a band does not have a distinct signature. The particles sink gravity-driven while recirculating within the pool and eventually join the sub-pool, wall-near region (red in Fig. 7) whereafter they re-emerge within the liquid layer on the cylinder's rising side.

Figures 8(a) and 8(b) display trajectories in planes $x - V_x$ and $V_y - y$ of phase space. The particle moves clockwise in Fig. 8(a) and anti-clockwise in Fig. 8(b). The superimposed dashed black ellipses in Figs. 8(a) and 8(b) represent the trajectory of a point at the inner cylinder surface. In the lower left quadrant ($x < 0$, $V_x < 0$) of Fig. 8(a) the light grey segments (red online) of the phase-space trajectory lie outside and below the dashed line. Hence, at these locations the V_x velocity component is more negative than that of the inner cylinder surface. This quadrant in phase space corresponds to the top half of the receding side of the cylinder in Fig. 1, where gravity drives a downward flow, resulting in higher azimuthal velocities relative to the surface of the rotating cylinder. The lower right quadrant ($x > 0$, $V_x < 0$) displays light grey (red online) segments of the phase-space trajectory with velocities values that are less negative than that of the inner surface of the rotating cylinder. This quadrant in phase space corresponds to the top half of the rising side

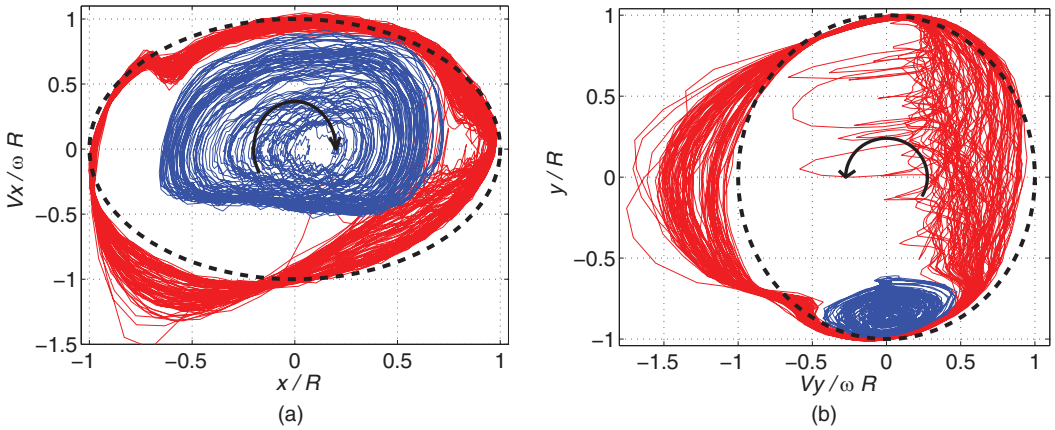

FIG. 8. Phase portrait in the (a) $x - V_x$ (b) $V_y - y$ coordinate planes for the run PT#1. Parts of the trajectory when the particle travels with a band appear grey (red online) and parts of the trajectory when the particle was contained within the pool appear black (blue online). The superposed dashed black line represents the phase-space trajectory of a hypothetical particle attached to the inner cylinder surface.

of the cylinder in Fig. 1 where gravity drives a downward flow, decelerating the liquid relative to the surface of the rotating cylinder. Similarly, the upper left and right quadrants of the phase-space trajectory in Fig. 8(a) correspond to, respectively, the lower left and the lower right quadrants of the cylinder in Fig. 1. Note that Fig. 8(a) reveals a sudden deceleration of particles as they enter the sub-pool region in the bottom half of the receding side of the cylinder as is apparent from the kink on the light grey (red online) segment of the phase-space trajectory in the vicinity of $x/R \approx -0.6$ mm, $V_x/\omega R \approx 0.6$ mm/s.

In the $V_y - y$ phase portrait, in Fig. 8(b), the right half of the figure corresponds to the rising part of the cylinder surface and the left half to its receding part. It can be seen that the V_y velocity component is reduced on the rising side of the cylinder and increased on the receding side due to the action of gravity. Similarly to Fig. 7, the loops protruding inwards from the right (rising) part of $V_y - y$ phase portrait are the signatures of oil droplets that had detached (fully or partially) from the liquid film to be re-entrained shortly afterwards. Signatures of the falling oil droplets (lines crossing the circle in Fig. 7) involve high vertical velocities and thus are outside the scale of the phase portrait $V_y - y$.

The most significant conclusion that can be drawn from Figs. 6–8 is that individual particles alternately reside either within granular bands or within the recirculating pool for extended periods of time. The two different particle states are associated with the two different regions of both physical and phase space.

It is interesting to extract profiles for the fluid velocity within the liquid film at the cylinder surface from the *PEPT* data and compare these to the theoretical profiles expected for a homogeneous liquid. Figure 9 displays radial profiles of the azimuthal velocity in the $x - y$ plane averaged over the periods when the tagged particle was contained within granular bands. The fluid velocity is plotted relative to the inner cylinder surface, i.e., with the constant value ωR subtracted. The experimentally measured profiles are shown in comparison with theoretical parabolic profiles for the flow of a granule-free liquid film coating the inner surface of the cylinder. Since the liquid layer on the inside of the cylinder surface does not exceed 2 mm in thickness, as can be estimated by inspecting the *PEPT* data in Fig. 7, the radial distance from the cylinder surface has been magnified by a factor of eight so that the profiles become clearly visible. Expectedly, Fig. 9 shows the presence of downward

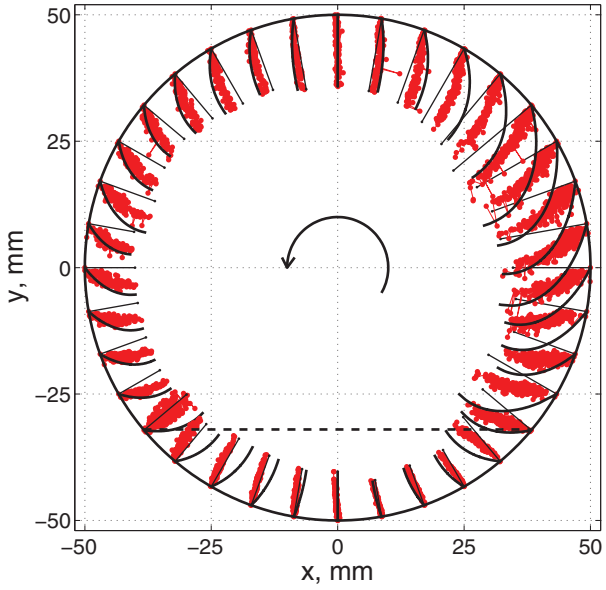

FIG. 9. Profiles of the experimentally measured azimuthal particle velocity while travelling with bands (grey, red online) compared to theoretical gravity-driven film-flow parabolic profiles (black solid lines) for the homogeneous carrier liquid. The fluid velocity is plotted relative to the inner cylinder surface, i.e., with the constant value ωR subtracted. The radial coordinate is magnified by a factor of 8 to provide a sufficiently clear resolution. The dotted horizontal line indicates the pool surface.

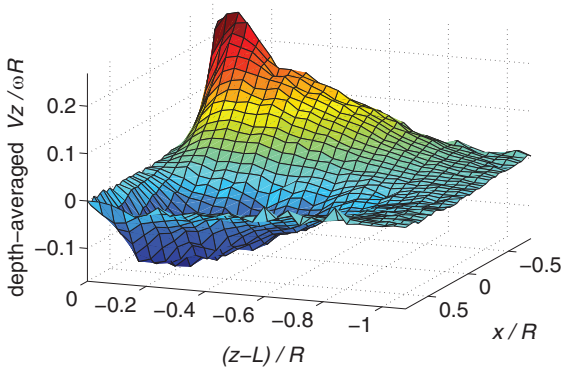

FIG. 10. Axial velocity near the cylinder end wall: $V_z/\omega R$ averaged over the pool depth in run PT#5.

flow, relative to the rotating cylinder surface, on both the rising and the receding side of the cylinder. The measured values of the flow velocities within the granular bands, relative to the inner cylinder surface, are less than those predicted for the homogeneous liquid and this reflects the increase of effective fluid viscosity within particle-rich regions.

The left and right end walls of the rotating cylinder are expected to drive local flows in the pool with strong axial flow components V_z. It is reasonable to assume that this local flow is responsible for the band drift. To investigate this issue, we determined the flow velocity in the wall-near region of one of the end walls from the *PEPT* data for periods when the tagged particle spent extended periods of time within the vicinity of the wall. Figures 10 and 11 display the axial velocity of the particle in the vicinity of the right end wall of the cylinder. The surface and contour plots shown in the figures were obtained by averaging data over tens of particle passages through 2×2 mm bins. Positive and negative values of V_z represent flow towards and away from the wall, respectively. Figure 10 displays values for V_z averaged over the pool depth. The figure provides clear evidence of the recirculating flow driven by the end walls. The influence of this recirculating flow on the drift of granular bands in the near-wall region will be discussed in Sec. IV. The figure also shows that the axial extent of the recirculating region is of the order of the cylinder radius; which is consistent with the low Reynolds number flow regime. The axial extent of this zone also agrees with the width of the wall-near zones referred to in the context of the discussion of the space-time diagrams in Refs. 6 and 7 and also clearly visible here in Fig. 12. Figure 11 displays a contour plot of the axial velocity in the $x - y$ plane at a distance of R/5 from the end wall; where the velocity has its maximum. The figure illustrates the spatial structure of the recirculating flow region in the vertical plane. The end wall is viewed head-on; the flow velocities are directed towards the viewer on the left (receding) side of the figure and away from the viewer on the right (rising) side.

To relate the particle dynamics to the band drift, the axial position z of the radioactively tagged particle has been superimposed onto the spatiotemporal plots illustrating the band drift in Figs. 12 and 13. The spatiotemporal image is obtained in a similar way as the spatiotemporal plots described in Refs. 6 and 7. Photographs of the cylinder, such as that in Fig. 2, were taken after time intervals of 1 min. Then pixel intensities were extracted along the same horizontal line in each photographs

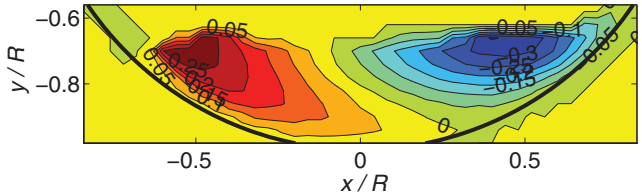

FIG. 11. Contour plot of the normalised axial velocity $V_z/\omega R$ in the $x - y$ plane at a distance of $R/5$ (10 mm) from the end wall in run PT#5.

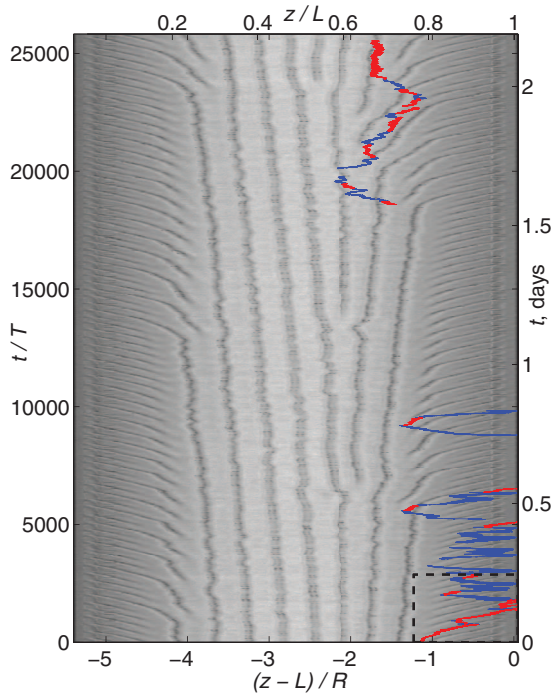

FIG. 12. Spatiotemporal image of the band-drift dynamics with superimposed trajectory of the tagged individual particle as measured by *PEPT* in run PT#3. The rectangular region in the bottom right corner of the figure, highlighted by the dashed line, is reproduced on a magnified scale in Fig. 13.

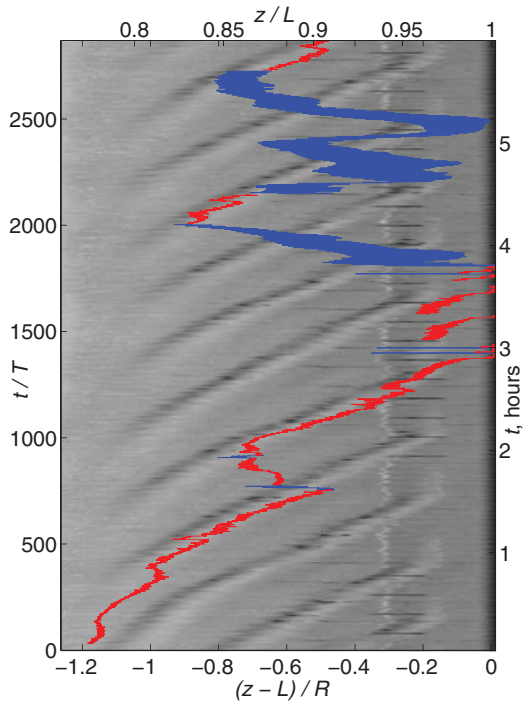

FIG. 13. Magnified lower right corner of the spatiotemporal diagram shown in Fig. 12 (run PT#3). The figure reveals that the particle travels with the band while periodically rising to the top of the cylinder (light grey, red online, parts of the trajectory) but it is uncoupled from the band pattern when staying in the pool (black, blue online, parts of the trajectory).

and these were then composed into the spatiotemporal diagram. Each horizontal line in the grey scale image corresponds to the band brightness at the instant the photograph was taken. Dark areas correspond to the particle-rich bands while light areas correspond to the particle-free zones. If the bands were stationary, the image would consist of vertical lines only. In Figs. 12 and 13 light grey (red online) segments of the trajectory identify intervals when the particle is in the close proximity of the inner surface of the cylinder, periodically rising to the top of the cylinder and then passing underneath the liquid pool. The black (blue online) segments of the trajectory identify intervals when the particle remains within in the liquid pool. Figure 12 shows the dynamics of the whole band pattern for the entire duration of the experiment while Fig. 13 displays a magnified view of the rectangular region marked by the dashed line in the bottom right-hand corner of Fig. 12.

Figures 12 and 13 and other similar spatiotemporal plots available from the *PEPT* experiments have revealed that the particle position reflects the large-scale motion of a band as long as the particle is associated with that band (red segments). However, when the particle remains within the pool (black parts of the trajectory, blue online) its drift is decoupled from that of the bands which is best illustrated in the near-wall region in Fig. 13.

IV. BAND DRIFT

The above discussions have revealed the flow structure near the end walls and have also shown that the particles often remain within granular bands following them for extended periods of time. This enables the near-wall band drift velocity to be related to the measured axial motion of the particles arising from the three-dimensional flow structure near to, and driven by, the cylinder end walls. We assume that the flow pattern in the pool is essentially steady and unaffected by the exact position of the bands.

Based on the data from Figs. 10 and 11, it is possible to obtain a rough estimate for the drift velocity of the granular bands. Figure 13 reveals that the the band-drift velocity is nearly constant within the interval between $0.8R$ and $0.2R$ from the end walls. Moreover, Figs. 10 and 11 suggest that a typical value of axial velocity in the end regions of the pool is 1/10 of the rotational velocity of the cylinder:

$$V_z \sim \omega R/10. \tag{1}$$

As the Reynolds number in most of our experiments is much less than 1 (cf. Table I) the assumption that the velocity is proportional to ω is reasonable. Due to the no-slip condition at the bottom of the pool, the vertical gradient of the axial velocity is approximately

$$\frac{\partial V_z}{\partial y} \sim \frac{\omega R}{10 \cdot h}, \tag{2}$$

where h is the depth of the pool as illustrated in Fig. 14. Particles contained in a granular band enter the pool at a certain distance above the bottom cylinder surface. Moving in azimuthal direction, they also get convected axially towards the end wall with the velocity V_z existing at that height above the bottom surface of the cylinder. While travelling in the bottom region of the pool the particles sink with the Stokes sedimentation velocity V_s. Thus, when the particles pass from the region with axial velocity directed towards the wall to the region with the axial velocity directed away from the end wall, they will have sunk closer to the bottom cylinder surface where the magnitude of V_z is lower (cf. Fig. 14). For the typical experimental conditions, the pool width is approximately equal to the cylinder radius R. Hence, the time that a particle is advected towards or away from the end wall is half of the time the particle spends within the pool, i.e., $\arccos(h/R)/\omega = \arccos(32/50)/\omega \sim 1/\omega$ (see Fig. 14). Within this time interval, the particle sinks by the distance of V_s/ω. Thus, the distance by which particles in the band and thus the band itself drift towards the end wall during one revolution is

$$\Delta z \sim \frac{\partial V_z}{\partial y}\frac{V_s}{\omega} \cdot \frac{1}{\omega}. \tag{3}$$

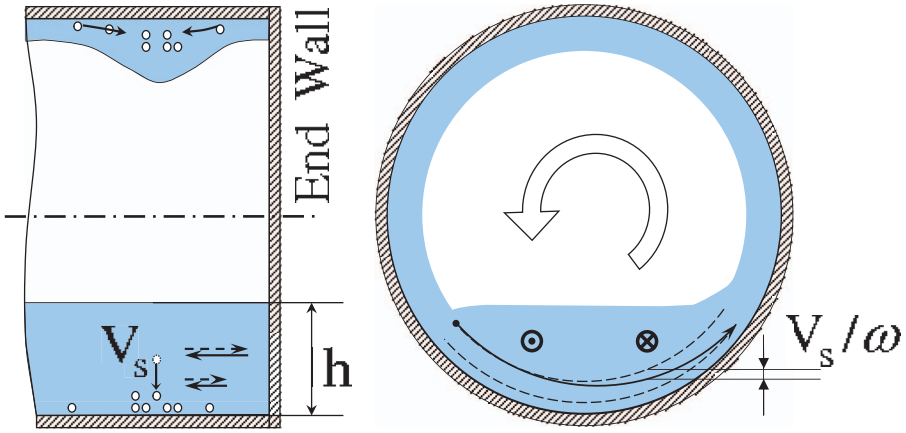

FIG. 14. Schematic of the band drift near the end wall. Dense particles sink towards the bottom cylinder surface during their motion within the pool. Upon entering the pool the axial flow advects particles stronger towards the end wall than they are advected away before exiting the pool.

Defining the band drift speed as $\Delta z/T$, where $T = 2\pi/\omega$, and using (2), we have

$$V_{drift} = \frac{\Delta z}{T} \sim \frac{\omega R}{10 \cdot h}\frac{V_s}{\omega} \cdot \frac{1}{\omega} \cdot \frac{\omega}{2\pi} \sim \frac{1}{2\pi}\frac{R}{10 \cdot h}V_s \approx \frac{V_s}{25}. \tag{4}$$

Note that the drift speed given by this expression does not depend on the rotation rate of the cylinder. Bands in Fig. 13 drift with the speed of 10 μm/s which is consistent with the value of approximately 12 μm/s given by (4) for the particle sink rate of 300 μm/s calculated for the run PT#3. The ratio V_{drift}/V_s determined from spatio-temporal diagrams of runs PT#1, PT#3, PT#4, and PT#5 is 0.078, 0.033, 0.031, and 0.044, respectively, which is not very different from the value of 0.04 predicted by (4).

The above considerations explain the mechanism of band drift in the vicinity of the end walls. The spatiotemporal diagram in Fig. 12 shows that the dynamics of bands located further than R from end walls differs considerably from the near-wall dynamics. Far from the walls, the band drift is slower by more than an order of magnitude and probably involves other mechanisms of band interaction mediated by surface tension and axial particle transport in the pool.

V. MECHANISM OF THE BAND FORMATION AND THE BAND GROWTH RATE

Jin and Acrivos[13,14] suggested a plausible mechanism for the band formation for the case of neutrally buoyant particles. Their model is based on the increased effective viscosity in regions of high particle concentrations that induce axial flow and an associated particle transport. Obviously, the mechanism described by Jin and Acrivos for neutrally buoyant particles is also relevant to the present experiments where the particles are denser than the liquid phase. However, dense particles are responsible for an additional mechanism that supports the granule-band formation as illustrated in Fig. 15. There exists the following band-formation feedback loop. A local increase in particle concentration at a point within the liquid film on the inner cylinder surface results in a locally increased film density. When a local maximum of the film density exists in the region of an overhanging part of the cylinder surface (approx location (A)-(B) in Fig. 15), gravity induces a flow that leads to further film thickening and thus further increase in the local particle concentration per unit area. At the upward-facing part of the layer (location (C) in Fig. 15), the overall action of gravity is to reverse the thickening and the increased particle concentration established while at the top of the cylinder. However, the distance from location (B) to the re-entry into the pool (D) is shorter than the distance between (A) and (B), and gravity does moreover accelerate fluid motion towards the pool. Consequently, the time fluid spends at the upward-facing part of the cylinder is small and the reversal flattening of the particle concentration does not have time to complete. When the particle-rich region

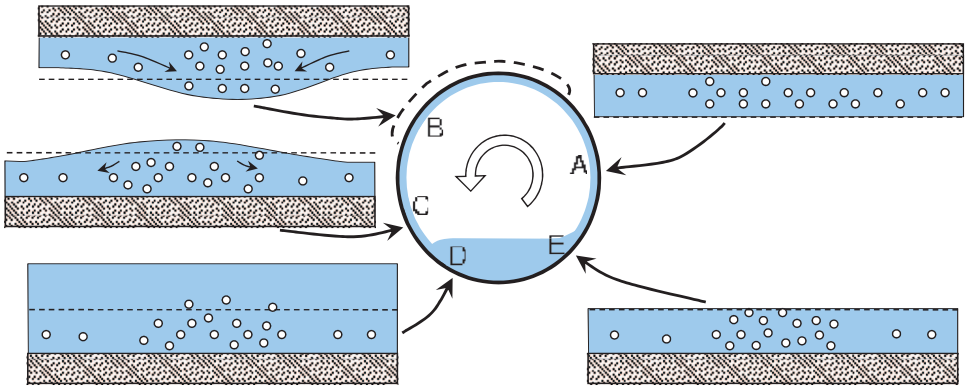

FIG. 15. Illustration of the mechanism of the band formation. An initial particle excess at the location (A) results in an increase of the film thickness on the inner cylinder surface while overhanging and moving from (A) to (B). As a result, the concentration of the particles per unit area of the layer increases further. As the layer spends less time being oriented upwards around (C), the bulge does not disappear during this phase. When submerged underneath the pool (D), particles do not move horizontally but only sink vertically. As a result, the amplified perturbation (increase in the particle concentration) re-emerges at the beginning of the next cycle (E) and, thus, a positive feedback loop is established.

enters the pool there no longer exists a free boundary and the restorative action of gravity is reduced so that the maximum in particle concentration remains almost unchanged between (D) and (E). Once the particle-rich region re-emerges from the pool on the rising side of the cylinder, it represents a spot for further preferential particle aggregation establishing a positive feedback loop. Similarly to the experiments by Jin and Acrivos[14] with neutrally buoyant particles, the existence of the pool is essential for the band formation. Once the bands have entered the pool they remain unmodified until their exit from the pool on the rising side of the cylinder.

To get an indirect confirmation that the band formation is related to the difference in particle motion above and below the pool surface, we calculate the standard deviation (*STD*) of the axial velocity V_z of the tagged particle while it is travelling within a band and while being located above or below the pool surface. Only parts of the trajectory located further than one cylinder diameter from the end walls were analyzed to avoid effects of the end walls. In the five experimental runs where the particle spent sufficiently long periods far from the end walls, PT#1-4 and PT#6, the ratio of $STD(V_z)$ above and below the pool surface is 1.5, 2.0, 1.23, 1.33, and 1.17, respectively. This is an indicator of more intense particle movement when outside the pool.

To obtain some quantitative data on the band formation, we have measured the growth rate of the optical intensity of the bands since this reflects the number of the granules entrained. The rotating cylinder was filmed as viewed in Fig. 2. The obtained images were Fourier-decomposed along the axial direction and the area of the main peak in the wavenumber space was calculated. The area of the peak in the Fourier spectrum represents the amplitude of the growing harmonic and its time derivative can be associated with the growth rate of granular bands. The result of the analysis of 16 runs is shown in Fig. 16 where the area of the Fourier peak is displayed in arbitrary units as a function of time. The thin solid lines and thick dashed lines represent data for particles with mean radius of $r_p = 80\,\mu$m and $r_p = 170\,\mu$m, respectively, and for each experiment the volume fraction of particles was the same (8%) as in the *PEPT* experiments. Each of the two groups of graphs for particles of the two different sizes contains lines for different cylinder rotation rates in the range from 3.2 rpm to 34 rpm. In Fig. 16 the gradient of the lines in the semi-logarithmic representation can be interpreted as the growth rate of the granular bands. The figure reveals that the band growth rate in different experiments falls into one of the two groups depending on the particle size. In other words, the growth rate of the bands is essentially independent of the rotation rate of the cylinder provided all other parameters, including the particle size, are kept constant. Suspensions containing particles with approximately 4.5 times higher sink rate were observed to form granular bands approximately 4 times faster. In both cases, bands form within the time exceeding the particle sink time from top to the bottom of the pool in the absence of the flow by a factor of approximately 10. This suggests

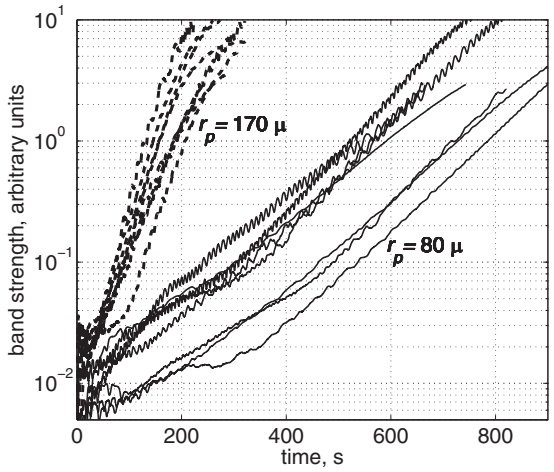

FIG. 16. Optically measured band intensity, in arbitrary units, as a function of time for cylinder rotation rates 3.2 rpm to 34 rpm of runs BG#38 . . . BG#45 and BG#47 . . . BG#54. Thin solid lines and thick dashed lines for suspensions carrying particles with mean radius $r_p = 80\,\mu$m and $r_p = 170\,\mu$m, respectively.

that in our experiments with heavy particles, the sedimentation plays a decisive role in the band growth.

The mechanism that was originally thought to be responsible for the band formation is shear-induced diffusion.[5,16] However, Jin and Acrivos[13,14] subsequently showed that this is not the case and our present data support their conclusion. To obtain an order-of-magnitude estimate for the expected band-formation rate due to shear-induced diffusion we use the particle diffusion coefficient reported by Breedveld *et al.*[15] For suspensions of up to 20% particle concentration they state a diffusion coefficient

$$D \sim 0.02\,\gamma\, r_p^2, \tag{5}$$

where γ is the shear rate. We estimate the typical shear rate based on the fact that the vertical flow speed in the liquid layer is at the level of $\omega R/2$ (see, for example, $V_y - y$ phase diagram in Fig. 8). When the bands are in the early stage of their growth (band strength, say, 10^{-1} in Fig. 16), we assume that the inhomogeneity of the vertical velocity in the axial direction is an order less than this velocity and, hence, does not exceed $\omega R/10$. Denoting the distance between bands as λ, one gets

$$\gamma \sim \frac{\omega R/10}{\lambda/2}. \tag{6}$$

Using (5) and (6) one estimates the time a particle requires to diffuse from the trough to the crest of particle concentration, i.e., to diffuse a distance equal to $\lambda/2$, as

$$\tau \sim \frac{(\lambda/2)^2}{D} \sim \frac{(\lambda/2)^2}{0.02\,\gamma\, r_p^2} \sim \frac{(\lambda/2)^3}{0.02\,\omega R/10\; r_p^2} \sim \frac{60\lambda^3}{\omega\, R\, r_p^2}. \tag{7}$$

It is worth noting that (7) suggests that the band-formation time increases as the inverse square of the particle size which is close to what is observed in Fig. 16. Moreover, the ratio λ^3/ω is approximately constant for the experiments shown in Fig. 16 and consequently the observed independence of the band growth rate on ω does not contradict (7). However, substituting parameters representing the middle of the range of the runs plotted in Fig. 16 (cylinder rotation rate, 9 rpm; $\lambda \sim 20$ mm as measured from video recordings; $r_p = 170\,\mu$m) one finds $\tau \sim 100$ hours while the tenfold growth of the band intensity in Fig. 16 occurs in less than 100 s. This result supports the conclusion that, similar to the case of neutrally buoyant particles,[13,14] shear induced diffusion is not responsible for the band formation in our experiments with particles denser than the ambient liquid.

VI. SUMMARY AND CONCLUSION

The measurements employing the *PEPT* technique have revealed that particles in a particle-laden rimming flow primarily reside in two different states. Particles spend extended periods of time either recirculating within the pool at the bottom of the rotating cylinder or being trapped within a granular band where they rise to the top of the cylinder on every revolution (Fig. 6). Particles can escape from a band either when the band disappears upon reaching the end wall of the cylinder or, alternatively, by falling into the pool inside droplets detaching from the liquid film near the top of the cylinder (Fig. 7). Particles trapped within bands and those staying in the pool occupy non-overlapping regions in phase space (Fig. 8). The present experiments have shown that the dynamics of individual particles is closely related to the band drift (Fig. 13). The two end walls establish recirculating flow in their vicinity with a substantial axial velocity component (Figs. 10 and 11) which induces the drift of granular bands towards the end walls (Fig. 14). Profiles of the azimuthal velocity within granular bands coating the inner cylinder wall were compared with the parabolic velocity profiles which would occur in the layer of a homogeneous liquid of the same thickness. It was found that the azimuthal fluid velocity in the particle-rich granular bands lags behind the corresponding values predicted for the particle-free film (Fig. 9). This has to be attributed to the increased effective fluid viscosity in particle-rich regions.

Jin and Acrivos[13,14] proposed a viscosity-based mechanism responsible for the formation of granular bands for the case of liquids carrying neutrally buoyant particles. For the present experiments with particles denser than the carrier liquid, we have suggested an additional density-based mechanism which can be responsible for the formation of the granular bands. Furthermore, the present *PEPT* study uncovered the mechanism responsible for the drift of the granular bands located in the vicinity of the end walls. However, our results do not explain the drift and the drift modes of granular bands in the central region of the cylinder where the dynamics is not directly governed by end-wall effects. We also emphasize that, due to the long timescales involved in conducting the type of *PEPT* experiments described here, the present study could only cover a very limited range within the overall parameter space (Table I) of the relevant nondimensional parameters discussed in Refs. 13 and 14 and Ref. 7.

In conclusion, the *PEPT* technique has demonstrated itself as a powerful tool to study aspects of particle-laden rimming flows that are unaccessible to other existing measurement techniques. However, *PEPT* experiments are resource-intense which restricted the number of experiments that could be conducted for the present study. Collecting statistical data on the chaotic particle-band dynamics would require prohibitively large resources. Many of the experiments by Guyez and Thomas[6,7] did, for instance, only reveal established spatiotemporal band-drift patterns after the system was observed for several days or even weeks. Consequently, analysis of the data collected for the present study could only address some of the basic aspects of the complicated spatiotemporal dynamics displayed by particle-laden rimming flows. Nevertheless, obtained results have enabled first insights into the dynamics of an individual particle in relation to the global dynamics of the system, explained the mechanism for the band drift close to end walls, and led to the suggestion of an additional mechanism leading to the formation of granular bands in the first place.

[1] G. Seiden and P. J. Thomas, "Complexity, segregation and pattern formation in rotating-drum flows," Rev. Mod. Phys. **83**, 1323–1365 (2011).
[2] B. A. Malkin, "The behaviour of condensate in paper machine dryers," The Dominion Engineer **4**(4), 8–11 (1937a).
[3] B. A. Malkin, "The behaviour of condensate in paper machine dryers (concluded)," The Dominion Engineer **4**(5), 8–10 (1937b).
[4] F. Melo, "Localized states in a film-dragging experiment," Phys. Rev. E **48**, 2704–2712 (1993).
[5] O. A. M. Boote and P. J. Thomas, "Effects of granular additives on transition boundaries between flow states of rimming flows," Phys. Fluids **11**, 2020–2029 (1999).
[6] E. Guyez and P. J. Thomas, "Spatiotemporal segregation-band drift in particle-laden rimming flow," Phys. Rev. Lett. **100**, 074501 (2008).
[7] E. Guyez and P. J. Thomas, "Effects of particle properties on segregation-band drift in particle-laden rimming flow," Phys. Fluids **21**, 033301 (2009).
[8] P. J. Thomas, G. D. Riddell, S. Kooner, and G. P. King, "Fine structure of granular banding in two-phase rimming flow," Phys. Fluids **13**, 2720–2723 (2001).

[9] D. J. Parker, C. J. Broadbent, P. Fowles, M. R. Hawkesworth, and P. McNeil, "Positron emission particle tracking - a technique for studying flow within engineering equipment," Nucl. Instrum. Methods Phys. Res., Sect. A **326**, 592–607 (1993).
[10] D. J. Parker, R. N. Forster, P. Fowles, and P. S. Takhar, "Positron emission particle tracking using the new birmingham positron camera," Nucl. Instrum. Methods Phys. Res., Sect. A **477**, 540–545 (2002).
[11] J. Seville, A. Ingram, X. Fan, and D. Parker, "Positron emission imaging in chemical engineering," Adv. Chem. Eng. **37**, 149–178 (2009).
[12] G. K. Batchelor, *Fluid Dynamics* (Cambridge University Press, Cambridge, 1967).
[13] B. Jin and A. Acrivos, "Rimming flows with an axially varying viscosity," Phys. Fluids **16**(3), 633–640 (2004).
[14] B. Jin and A. Acrivos, "Theory of particle segregation in rimming flows of suspensions containing neutrally buoyant particles," Phys. Fluids **16**(3), 641–651 (2004).
[15] V. Breedveld, D. V. D. Ende, A. Tripathi, and A. Acrivos, "The measurement of the shear-induced particle and fluid tracer diffusivities in concentrated suspensions by a novel method," J. Fluid Mech. **375**, 297–318 (1998).
[16] M. Tirumkudulu, A. Tripathi, and A. Acrivos, "Particle segregation in monodisperse sheared suspensions," Phys. Fluids **11**, 507–509 (1999).